



Dioxygen-enhanced CO₂ photoreduction on TiO₂ supported Cu single-atom sites

Ting Wang^{a,1}, Fuli Sun^{b,1}, Shoujie Liu^c, Guilin Zhuang^{b,*}, Benxia Li^{a,*}

^a Department of Chemistry, Key Laboratory of Surface & Interface Science of Polymer Materials of Zhejiang Province, Zhejiang Sci-Tech University, Hangzhou 310018, PR China

^b College of Chemical Engineering, Zhejiang University of Technology, Hangzhou 310014, PR China

^c Guangdong Laboratory of Chemistry and Fine Chemical Engineering, Shantou 515063, PR China

ARTICLE INFO

Keywords:

Photocatalytic CO₂ reduction
Cu active sites
Enhanced performance
Dynamic stability
In situ characterizations

ABSTRACT

Supported Cu single-atom (Cu-SA) catalysts have exhibited unique activity and selectivity in CO₂ reduction, but they generally suffer from the easy transformation of active Cu^{δ+} into inactive Cu⁰. Herein, porous TiO₂ supported Cu single atoms (Cu-SAs/TiO₂) photocatalyst was fabricated and dioxygen (O₂) enhanced photocatalytic CO₂ reduction performance of Cu-SAs/TiO₂ was investigated by *in-situ* characterizations and theoretical calculations. The results showed that both activity and stability of Cu-SAs/TiO₂ photocatalyst could be improved by feeding a small amount of O₂ (117.6 ppm) in the reaction system. The competitive electron transfer to O₂ on Cu-SAs/TiO₂ maintained dynamic stability of Cu^{δ+} active sites, and O₂-derived *OOH species lowered the formation energy barrier of key intermediate *COOH as well as delivered *H species for accelerating intermediates protonation process. Total yield rate of CH₄ and CO reached 34.64 μmol·g_{cat}⁻¹·h⁻¹ for CO₂ photoreduction over Cu-SAs/TiO₂ after introducing 117.6 ppm O₂, accompanied by enhanced durability.

1. Introduction

Recycling CO₂ into carbon fuels will become a dominant trend to alleviate serious climate change and deal with growing energy demand in the coming years [1,2]. Artificial photosynthesis with the aid of a photocatalyst can convert CO₂ into valuable fuels and chemicals using H₂O as an electron donor, which represents an attractive alternative strategy for large-scale CO₂ conversion under ambient condition [3,4]. The solar-driven CO₂ conversion *via* artificial photosynthesis requires an efficient photocatalyst that generally consists of light-harvesting units and catalytically active sites to synergistically work together, affording the photogenerated charge carriers with sufficient redox potentials as well as facilitating the adsorption and activation of CO₂ and H₂O molecules [5–8]. Particularly, the active sites on the surface of photocatalysts play crucial roles in promoting CO₂ reduction, such as enhancing CO₂ adsorption, capturing photogenerated electrons, lowering the reaction activation energy, and improving the product selectivity by altering absorption energies of intermediates [9,10]. The metal single atoms anchored on semiconductors have been verified as efficient active sites for CO₂ reduction in recent years because their

coordinately unsaturated configuration and unique electronic structures can regulate the affinities with reactants, intermediates and/or products as well as accumulate electrons by chemical valence states to supply sufficient electrons for CO₂ reduction [11–14]. Despite the achievements in developing the photocatalysts with single-atom active sites for CO₂ reduction, the lack of substantial information on the dynamic variations of active sites under practical conditions limits the understanding of photocatalytic CO₂ reduction process. Therefore, the scalable fabrication of photocatalysts with precisely designed metal single-atom active sites and the in-depth understanding of their photocatalytic behaviors in CO₂ reduction reaction are of extraordinary significance.

Atomically dispersed Cu active sites have showed favorable catalysis in converting CO₂ into hydrocarbons, because of their proper binding ability with CO₂ and reaction intermediates [4,15]. However, photocatalysts with Cu single-atom sites generally suffer from the reduction of Cu^{δ+} species to metallic Cu⁰ under a long-term photocatalytic process, which has triggered distressing issues such as short catalyst lifetimes, unstable product distribution, and uncontrollable reaction pathways [16]. *In-situ* X-ray absorption spectroscopy (XAS) analysis indicated that Cu²⁺ was beneficial to CO₂ adsorption while Cu⁺ could promote CO₂

* Corresponding authors.

E-mail addresses: glzhuang@zjut.edu.cn (G. Zhuang), libx@zstu.edu.cn (B. Li).

¹ T.W. and F.L.S. contributed equally to this work.

activation [17]. A recent study has evidenced that the initial Cu^{2+} species on TiO_2 could be gradually reduced to Cu^+ by the photogenerated electrons and ultimately to Cu^0 under light irradiation, in which a substantial presence of Cu^+ was more favorable for CO_2 to CH_4 conversion than the initial Cu^{2+} and the ultimate Cu^0 , and the photocatalytic activity declined significantly when Cu^0 was dominant in the photocatalyst after a prolonged irradiation time (4 ~ 6 h) [18]. A reported single-atom Cu/TiO_2 photocatalyst remained in active state until all Cu^{2+} was converted to Cu^{1+} which was further reduced to Cu^0 under light irradiation [19]. This change in the oxidation state of Cu could be reversed by exposing the catalyst to air until its dark color changed to white. Our recent study also showed that the continuous photocatalytic reaction caused an obvious decrease in the activity of $\text{Cu}^{\delta+}/\text{CeO}_2\text{-TiO}_2$ photocatalyst, but the activity could be mostly recovered after the photocatalyst was exposed in air [20]. Although *in situ*/operando characterizations have demonstrated that the dynamically survived Cu^+ species on catalyst surfaces might act as the active sites in affecting the activity/selectivity of CO_2 reduction [21,22], how to maintain the dynamic stability of Cu^+ sites on catalyst surface under practical conditions remains a great challenge for acquiring a long-term stable performance in photocatalytic CO_2 reduction. It has been observed that the rate of photocatalytic CO_2 reduction to CO over Cu/TiO_2 decreased with time but could be improved when performing the reaction in the presence of O_2 [23]. However, the mechanism that governs the improvements in photocatalysis remains a topic of considerable explorations, especially regarding the reaction path of O_2 as well as the roles of oxygen-containing intermediates in the photocatalytic CO_2 reduction process. In this regard, more substantial information on the surface species of photocatalysts should be directly extracted under practical reaction conditions by *in situ* spectroscopic characterizations together with theoretical calculations, to establish a direct correlation between photocatalyst surface speciation and reactivity, which would provide instructional guidance for rationally designing and constructing photocatalytic systems for solar-driven CO_2 conversion.

This work demonstrates a scalable fabrication of Cu single-atom (Cu-SAs) active sites anchored on porous TiO_2 , and reveals the O_2 induced enhancement in activity and stability of Cu-SAs/ TiO_2 catalyst for photocatalytic CO_2 reduction with H_2O as a proton/electron donor. A series of *in situ* characterizations and theoretical calculations demonstrate that the appropriate adsorption of O_2 on photocatalyst surface can suppress the reduction of $\text{Cu}^{\delta+}$ active sites to inactive Cu^0 through the electron transfer from Cu sites to chemisorbed O_2 , thus maintaining the dynamic stability of $\text{Cu}^{\delta+}$ for photocatalytic CO_2 conversion. Moreover, the generated- O_2 radical promotes H_2O dissociation to form $^*\text{OOH}$ intermediate which accelerates the proton-coupled electron transfer (PCET) process of CO_2 photoreduction. The performance of Cu-SAs/ TiO_2 catalyst is remarkably improved in a long-term photocatalytic CO_2 reduction process with adding a small amount of O_2 (117.6 ppm) in the reaction system.

2. Experimental section

2.1. Chemicals and reagents

Copper nitrate trihydrate ($\text{Cu}(\text{NO}_3)_2 \cdot 3\text{H}_2\text{O}$), titanium tetrakisopropylate (TTIP), 2-aminobenzene-1,4-dicarboxylate (BDC-NH_2), 5,5-dimethyl-1-pyrroline-N-oxide (DMPO), catalase (≥ 200000 unit/g), mannitol, superoxide dismutase (SOD) (≥ 1400 units/mg), 3,3',5,5'-tetramethylbenzidine (TMB), acetate (HAc), sodium acetate anhydrous (NaAc), methanol, sodium sulfate anhydrous (Na_2SO_4), potassium iodide (KI), potassium hydrogen phthalate ($\text{C}_8\text{H}_5\text{KO}_4$), deuterium oxide (D_2O) and N,N-dimethylformamide (DMF) were purchased from Aladdin Biochemical Technology Co. Ltd. All the chemicals were used without further purification.

2.2. Synthesis of Cu-SAs/ TiO_2 photocatalyst

For a typical synthesis, 0.2 g of the MIL-125- NH_2 metal-organic framework precursor synthesized according to our previously reported recipe [24] was dispersed in 20 mL $\text{Cu}(\text{NO}_3)_2$ aqueous solution with Cu^{2+} concentration of 0.25, 0.63 and 1.00 $\text{mmol}\cdot\text{L}^{-1}$, respectively. After 8 h magnetic stirring at room temperature, the solid was collected by centrifugation and dried at 60 °C, obtaining the $\text{Cu}^{2+}/\text{MIL-125-NH}_2$ precursors. The $\text{Cu}^{2+}/\text{MIL-125-NH}_2$ precursors were calcined at 450 °C for 3 h in air, with a heating rate of 1 °C/min, to obtain the Cu-SAs/ TiO_2 photocatalysts. Herein, the Cu-SAs/ TiO_2 photocatalyst obtained from the precursor that was prepared by impregnating MIL-125- NH_2 in the solution with Cu^{2+} concentration of 0.63 $\text{mmol}\cdot\text{L}^{-1}$ is the optimal one, and the Cu-SAs/ TiO_2 photocatalyst mentioned in this work is this sample unless otherwise specified.

2.3. Characterizations

The Cu contents of $\text{Cu}^{2+}/\text{MIL-125-NH}_2$ precursors and Cu/ TiO_2 photocatalysts were measured by atomic absorption spectrometry (AAS, Shimadzu AA-7000). The crystalline phases of all samples were characterized by powder X-ray diffraction (XRD, DX-2700 X-ray diffractometer) with monochromatized Cu K α radiation ($\lambda = 1.5406$ Å). The morphologies, microstructures and element distributions were analyzed by field-emission scanning electron microscope (FESEM, ZEISS Ultra-55), transmission electron microscope (TEM, JEL-2100) equipped with an electron energy-dispersive spectroscopy (EDS). The atomically dispersed Cu species was observed by the aberration-corrected high angle annular dark field scanning transmission electron microscopy (AC-HAADF-STEM) on a JEOL ARM200CF fifth order 4 AC-TEM. The X-ray absorption fine structure (XAFS) spectra data (Cu K-edge) were recorded at 1W1B station in Beijing Synchrotron Radiation Facility (BSRF, electron storage ring operated at 2.5 GeV with a maximum current of 250 mA) and Anhui Absorption Spectroscopy Analysis Instrument Co. Ltd of RapidXAFS 2 M. Cu foil and bulk CuO were used as the reference samples. XAFS data were processed by Athena and Artemis software, according to the standard procedures. X-ray photoelectron spectroscopy (XPS) measurements were performed on a Thermo Fisher Scientific K-Alpha spectrometer by using monochromated Al K α radiation (1486.6 eV), and the C 1 s peak at 284.8 eV was used as the reference for calibration. The specific surface areas and the pore size distributions of catalysts were determined by N_2 adsorption/desorption process on a Micromeritics ASAP 2020 v4.01 analyzer at 77 K, according to Brunauer-Emmett-Teller (BET) and Barrett-Joyner-Halenda (BJH) models, respectively. UV-visible diffuse reflectance spectra (DRS) were recorded on a Shimadzu UV-2600 spectrophotometer with BaSO_4 as a reference sample. The photoluminescence (PL) spectra were measured on HORIBA fluoromax-4 spectrophotometer by using the excitation wavelength of 300 nm. The electron paramagnetic resonance (EPR) spectra were measured on a Bruker model JEOL JES-FA200 spectrometer, with using the same quartz capillary tubes for all sample testing. The reactive radicals generated during the photocatalytic process were identified by *in situ* EPR detections, using 5,5-dimethyl-1-pyrroline-N-oxide (DMPO) as a radical-trapping reagent.

2.4. Photocatalytic CO_2 reduction tests

A double-walled quartz reactor (170 mL) was used for the photocatalytic CO_2 reduction reaction. Firstly, 5 mg of photocatalyst was dispersed ultrasonically in 800 μL ethanol to form a slurry, which was coated on a pre-cleaned glass slide (2.5 cm \times 2.5 cm) and then dried at 60 °C overnight. Ethanol was used to prepare the catalyst slurry because its lower surface tension is beneficial to the formation of uniform catalyst film on the glass slide, and the ethanol could be completely removed by drying at 60 °C overnight. The glass slide coated with catalyst was placed at the bottom of the quartz reactor, and 1 mL deionized water was

dropped near the glass slide. The pure CO₂ gas (or CO₂ gas mixed with a small amount of O₂) was blown into the reactor for 30 min. Subsequently, the sealed reactor was illuminated by a Xe lamp (PLS-SXE300, Beijing Perfectlight) which could provide the simulated sunlight with a main wavelength range of 320~850 nm and an optical power density of 200 mW·cm⁻². During photocatalytic process, the gas products were analyzed quantitatively by a gas chromatograph (GC 9790II, FuLi) equipped with both thermal conductivity detector (TCD) and flame ionization detector (FID) via an external standard method. For the cyclic test, the reactor was pumped and refilled with CO₂ gas mixed with a small amount of O₂ (117.6 ppm) before each new photocatalytic cycle began. The isotope-labeled photocatalytic experiment was carried out under the same conditions except that ¹³CO₂ was used to replace ¹²CO₂ and the products (¹³CH₄ and ¹³CO) were analyzed by gas chromatography-mass spectrometry (GC-MS, 7890A-5975 C, Agilent) system.

2.5. In situ DRIFTS measurements

The diffuse reflectance infrared Fourier transform spectroscopy (DRIFTS) was conducted on the Bruker TENSOR II FTIR spectrometer equipped with a liquid nitrogen-cooled mercury-cadmium-tellurium (MCT) detector. For the *in-situ* CO-DRIFTS measurements of probing Cu sites on photocatalyst, 40 mg photocatalyst was loaded in the chamber and pretreated in Ar atmosphere at 150 °C for 30 min. After the sample was cooled to room temperature in continuous Ar purging, the background spectrum was recorded. Subsequently, the sample was exposed to 10 vol% CO/Ar mixed gas (or 10 vol% CO/Ar mixed gas with addition of 117.6 ppm O₂) to achieve the adsorption-desorption equilibrium on photocatalyst. Then the sample was purged by pure Ar gas until the recorded spectrum remained unchanged. Finally, the infrared spectra were recorded in real time under the irradiation of Xe lamp to track the evolution of Cu sites. For the *in-situ* DRIFTS measurements to study photocatalytic CO₂ reduction process, 40 mg of the photocatalyst was loaded on the sample holder in the chamber, followed with the pretreatment in pure Ar atmosphere at 150 °C for 30 min. After the sample was cooled to room temperature in continuous Ar flow, the background spectrum was recorded. Subsequently, the humid CO₂ gas (or humid CO₂ gas mixed with a small amount of O₂) was blown into the chamber. After reaching adsorption-desorption equilibrium, the infrared spectra were recorded in real time under the illumination of Xe lamp.

2.6. The identification of reactive oxygen species generated during photocatalytic CO₂ reduction reaction

The reactive oxygen species (ROSs, such as O₂, OH and H₂O₂) generated during photocatalytic CO₂ reduction reaction were identified by using 3,3',5,5'-tetramethylbenzidine (TMB) as an indicator [25]. In a typical reaction, 15 mg TMB was dispersed in 30 mL HAC-NaAc buffer aqueous solution (pH = 5.0), followed by adding 100 μL aqueous suspension of Cu-SAs/TiO₂ catalyst (5 g·L⁻¹). After the pure CO₂ gas (or pure O₂ gas, or the CO₂ gas with addition of 117.6 ppm O₂) was bubbled into the reaction suspension for 30 min, the suspension was illustrated by Xe lamp with a power density of 200 mW·cm⁻². The UV-vis absorption spectra of reaction solution were measured after different irradiation time. In addition, the control experiments with adding different scavengers were performed according the same procedures described above. The scavengers added in the reaction system are superoxide dismutase (2000 unit/mL, 2 mL), mannitol (10 mg) and catalase (3500 unit/mL, 2 mL), to eliminate superoxide radical (·O₂), hydroxyl radical (·OH) and H₂O₂, respectively.

2.7. Detection of H₂O₂ produced during photocatalytic CO₂ reduction reaction

The H₂O₂ produced in photocatalytic CO₂ reduction reaction was

determined by a colorimetric method [26]. The chromogenic solution was composed of potassium hydrogen phthalate (C₈H₅KO₄) aqueous solution (3 mL, 0.1 M), potassium iodide (KI) aqueous solution (3 mL, 0.4 M) and 3 mL H₂O. After the photocatalytic CO₂ reduction reaction, the photocatalyst was immersed into the chromogenic solution for 5 min, where H₂O₂ could quantitatively react with I⁻ ions to produce I₃ ions. Then, the solution was filtered through a syringe filter to remove the catalyst particles, and the UV-vis absorption spectrum of filtrate was measured on a Shimadzu UV-2600 spectrophotometer. The corresponding amount of H₂O₂ was calculated according to the amount of I₃ determined by the characteristic absorption at 350 nm.

2.8. Computational methods

All density functional theory (DFT) calculations were performed with the Vienna Ab initio Simulation Package (VASP). The exchange correlation (XC) part in the Kohn–Sham equation was described by Perdew Burke Ernzerhof (PBE) functional in terms of the gradient of electronic density. The projector-augmented wave (PAW) pseudopotential, featuring the greater computational efficiency of plane wave as well as high accuracy of ultrasoft pseudopotential, was employed in the treatment of the ion-electron interaction. Plane wave function with kinetic energy less than E_{cut} of 450 eV is included in the basic set. The sampling of Brillouin zone adopted the k-mesh of $4 \times 4 \times 1$ grid for geometrical optimization and transition states calculations, and $10 \times 10 \times 1$ grid for single-point energy and all electronic properties calculations, having enough accuracy to total energy by convergence test. For self-consistent field (SCF) calculations, the stopping criterion was set to the energy difference less than 1.0×10^{-5} eV, while for geometrical optimization the convergence will reach until the Hellmann–Feynman force per atom less than 0.02 eV/Å. To correct the field Coulomb interaction in DFT calculation, $U = 4.0$ eV for Ti 3d state and $U = 7.0$ eV for Cu 3d state were utilized in the calculations. Moreover, DFT-D3 method was used to correct the Van der Waals force, and a vacuum layer of 20 Å along z axis was employed to prevent the interaction between two unit cells. The adsorption energy of reaction species was typically evaluated following the formula:

$$E_{\text{ads}} = E_{\text{total}} - (E_{\text{sub}} + E_{\text{mol}}) \quad (1)$$

where E_{total} , E_{sub} and E_{mol} are corresponding total energy of adsorption structure, catalyst and adsorbent. And the formation energy of oxygen vacancy is estimated according to this formula:

$$E_{\text{OV}} = E_{\text{OV-Cu-SA/TiO}_2} - E_{\text{Cu-SA/TiO}_2} + \frac{E_{\text{O}_2}}{2} \quad (2)$$

where $E_{\text{OV-Cu-SA/TiO}_2}$ and $E_{\text{Cu-SA/TiO}_2}$ are the energy of Cu-SA/TiO₂ catalyst with oxygen vacancy and the energy of original Cu-SA/TiO₂, respectively. E_{O_2} is the energy of gas-phase O₂. Transition states were identified by the Climbing Image-Nudged Elastic Band (CI-NEB) strategy. Gibbs free energies for each gaseous and adsorbed species were calculated at 298.15 K, according to the expression:

$$G = E_{\text{DFT}} + E_{\text{ZPE}} - TS \quad (3)$$

$$E_{\text{ZPE}} = \sum_i 1/2 h\nu_i \quad (4)$$

$$\Theta_i = h\nu_i / k_B \quad (5)$$

$$S = \sum_i R [\ln(1 - e^{-\Theta_i/T})^{-1} + \Theta_i/T (e^{-\Theta_i/T} - 1)^{-1}] \quad (6)$$

where E_{DFT} is the total energy, E_{ZPE} is the zero-point energy, S is the entropy (for free molecules, the translational, rotational, and vibrational entropy terms were considered, whereas for adsorbates, only vibrational entropy was taken into account due to the negligible contributions of the translational and rotational entropies) and T is the temperature (298.15 K). h is the Planck constant, ν is the computed vibrational frequencies, θ is the characteristic temperature of vibration, k_B is the

Boltzmann constant, and R is the molar gas constant. For adsorbates, all 3 N degrees of freedom were treated as frustrated harmonic vibrations with negligible contributions from the catalysts' surfaces.

3. Results and discussion

3.1. Material synthesis and characterization

The synthesis of Cu-SAs/TiO₂ photocatalyst (Fig. 1a) is implemented via the adsorption of Cu²⁺ ions into MIL-125-NH₂ and the pyrolytic transformation of Cu²⁺/MIL-125-NH₂ precursor in air, where Cu single-atom sites are *in situ* anchored in porous TiO₂ owing to the confinement effect and strong metal-support interaction [27]. The Cu contents of Cu²⁺/MIL-125-NH₂ precursors and Cu/TiO₂ photocatalysts are measured by atomic absorption spectrometry (AAS), as shown in Table S1 (Supporting Information), in which the optimal Cu-SAs/TiO₂ photocatalyst has 1.58 wt% Cu content. The X-ray diffraction (XRD) pattern of Cu-SAs/TiO₂ (Fig. S1a) shows only characteristic peaks of anatase TiO₂ (JCPDS-71-1116), without any peak of Cu species. It is noted that the (101) diffraction peak of TiO₂ in Cu-SAs/TiO₂ sample shifts a little to the larger 2θ value (Fig. S1b), compared with that of pure TiO₂, meaning the replacement of some Ti atoms by the smaller Cu atoms. The microstructures of Cu-SAs/TiO₂ photocatalyst are built by numerous small nanoparticles to present porous feature (Fig. S1c-d)

which is confirmed by N₂ isothermal sorption-desorption measurement (Fig. S2). In the aberration-corrected high-angle annular dark-field scanning transmission electron microscopy (AC-HAADF-STEM) images (Fig. 1b and Fig. S1e-f), some isolated bright spots marked by white circles are distinguished from the surrounding atoms of TiO₂ matrix, corresponding to the Cu single atoms which are heavier a little than Ti atoms. No Cu or CuO clusters/particles are observed, indicating that Cu is atomically dispersed on TiO₂ support. The darker regions around Cu atoms (Fig. 1b) suggest the defective structure of TiO₂ support [28], and the defect-rich surface created by Cu doping can afford abundant coordination-unsaturated sites for chemisorption of reactant molecules. STEM-associated energy-dispersive spectra (EDS, Fig. 1c) further affirm the homogeneous distribution of Cu atoms on TiO₂.

The element-selective X-ray absorption fine structure (XAFS) spectra depict the local coordination structure of Cu atoms in Cu-SAs/TiO₂ catalyst. As shown in Fig. 1d, the Cu-SAs/TiO₂ sample shows a similar Cu K-edge X-ray absorption near edge structure (XANES) profile with that of CuO, and the absorption peak at 8996.5 eV is characteristics of positive Cu²⁺/Cu⁺ ions [19]. However, the obvious difference in Cu K-edge XANES profiles between Cu-SAs/TiO₂ and CuO indicates that the coordination environment of isolated Cu^{δ+} in TiO₂ is different from that of Cu²⁺ in CuO [29]. The atomically dispersed Cu^{δ+} in TiO₂ is further confirmed by the extended X-ray-absorption fine-structure (EXAFS) analysis (Figs. 1e and S3). The Cu K edge EXAFS spectrum of

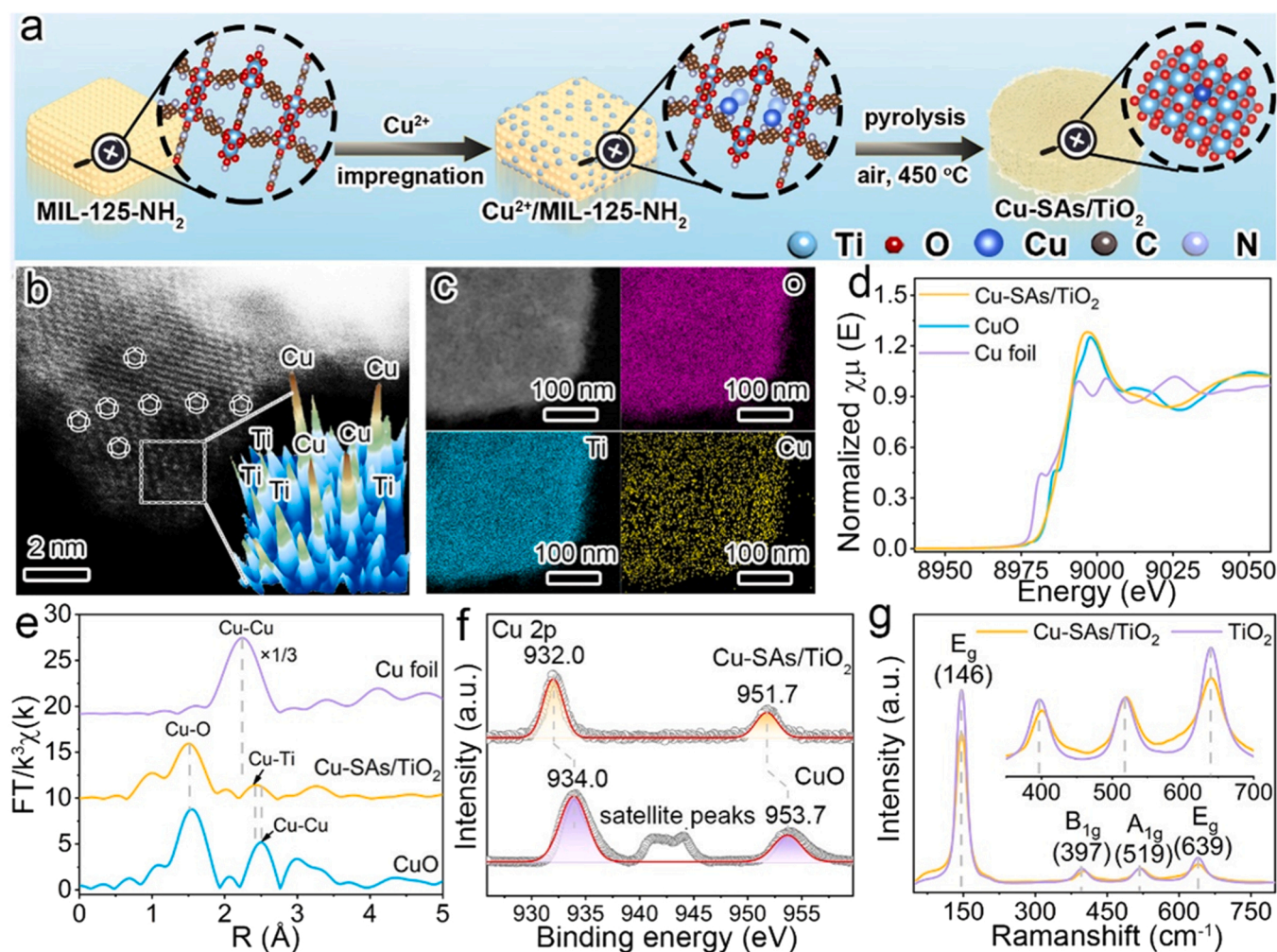


Fig. 1. (a) Schematic diagram of Cu-SAs/TiO₂ photocatalyst synthesis. (b) AC-HAADF-STEM image (insert is the intensity profiles taken from the rectangle-marked area). (c) HAADF-STEM image and the corresponding EDS element mappings of Cu-SAs/TiO₂ sample. (d) Normalized Cu K-edge XANES spectra and (e) FT-EXAFS spectra of Cu-SAs/TiO₂, Cu foil and bulk CuO. (f) XPS spectra of Cu-SAs/TiO₂ and bulk CuO. (g) Raman spectra of Cu-SAs/TiO₂ and pure TiO₂ (insert is the enlarged view from 350 to 700 cm⁻¹).

Cu-SAs/TiO₂ presents a main peak stemmed from the direct binding of Cu atoms with lattice oxygen (Cu–O) as well as a minor peak originated from Cu–Ti contribution, suggesting the local TiO₂ environment around the isolated Cu atoms [19]. The characteristic peak belonging to Cu–Cu bonding is not observed, excluding the existence of metallic Cu⁰ in Cu-SAs/TiO₂ catalyst [30]. X-ray photoelectron spectroscopy (XPS) is further used to probe the chemical states of surface species of Cu-SAs/TiO₂ catalyst. Since the existence of metallic Cu⁰ in Cu-SAs/TiO₂ has been excluded by XAFS analysis, the peaks at 932.0 and 951.7 eV in Cu 2p spectrum of Cu-SAs/TiO₂ (Fig. 1f) are ascribable to 2p_{1/2} and 2p_{3/2} of Cu⁺ ions [31]. In comparison to the Cu 2p spectrum of CuO reference sample, the negative shift in binding energies of atomically dispersed Cu⁺ is ascribable to the strong electronic interaction between

single Cu atoms and the surrounding TiO₂ [4]. The O 1s spectrum of Cu-SAs/TiO₂ (Fig. S4) can be divided into two peaks related to the lattice oxygen (O_L) at ~ 529.7 eV and the adsorbed oxygen on oxygen vacancies (O_V) at ~ 531.3 eV [32], respectively. The local structural variation of TiO₂ after introducing Cu SAs are further characterized by Raman spectroscopy. Both TiO₂ and Cu-SAs/TiO₂ present the similar peaks at 146, 397, 519, and 639 cm⁻¹, as shown in Fig. 1g, indicating the typical anatase TiO₂ phase [33,34]. No Raman characteristic peaks of CuO appear for Cu-SAs/TiO₂ sample, which is consistent with the dispersed state of isolated Cu atoms in TiO₂. The E_g peaks correspond to symmetric stretching vibration of O–Ti–O, while the B_{1g} peak is related to symmetric bending vibration of O–Ti–O, and the A_{1g} peak (519 cm⁻¹) is resulted from antisymmetric bending vibration of O–Ti–O [33]. The

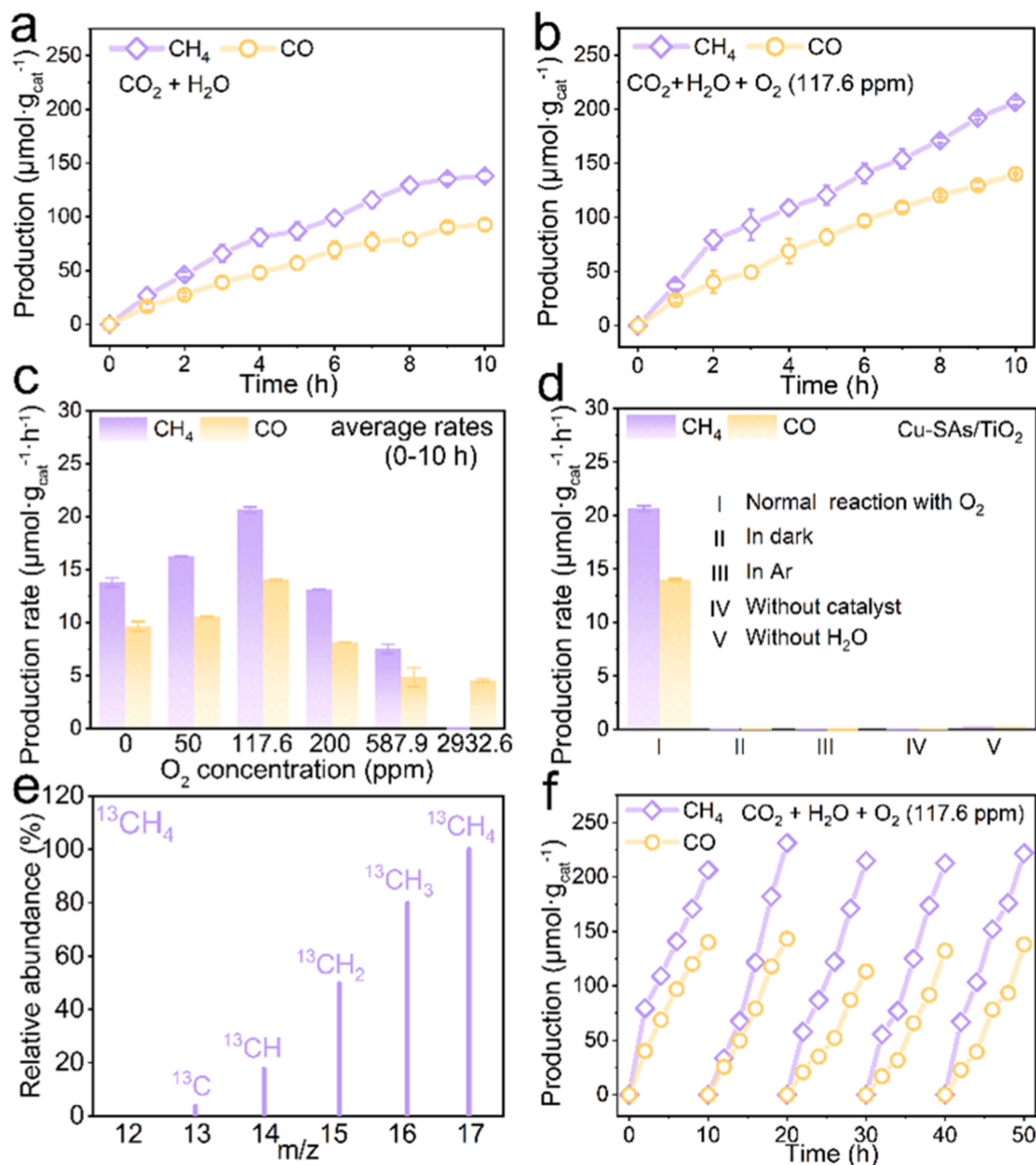


Fig. 2. Photocatalytic CO₂ reduction over Cu-SAs/TiO₂. Product evolutions in the reaction system with O₂ concentration of (a) 0 ppm and (b) 117.6 ppm, (c) the average evolution rates of CH₄ and CO for 10 h photocatalytic reaction with different O₂ concentrations; (d) control experiments under different conditions, (e) mass spectrum of CH₄ extracted from GC-MS analysis of isotope labeling experiment with ¹³CO₂ replacing ¹²CO₂, (f) the cycling experiments of Cu-SAs/TiO₂ photocatalyst for CO₂ reduction in the presence of 117.6 ppm O₂ with each cycle for 10 h.

decreased intensities of E_g and B_g peaks mean the reduced symmetric stretching vibration and bending vibration modes of O-Ti-O in TiO_2 after introducing Cu SAs. The broadening and shift of B_{1g} peak at 397 cm^{-1} for Cu-SAs/ TiO_2 (insert of Fig. 1g) compared with that of pure TiO_2 , suggesting the local structural distortion of TiO_2 caused by the introduction of Cu atoms [35].

According to UV–vis diffuse reflectance spectroscopy (UV-DRS), the Cu-SAs/ TiO_2 sample exhibits distinct light response in visible region (Fig. S5a), in comparison to pure TiO_2 . The band in the region of 400–600 nm is ascribable to the charge transfer from O 2p valence band of TiO_2 to $\text{Cu}^{\delta+}$ [36]. The enhanced photoabsorption from 600 to 800 nm is attributable to the transition between d-d orbitals of $\text{Cu}^{\delta+}$ ions as well as the presence of defect levels [23,34]. Besides, the Cu-SAs/ TiO_2 sample shows a remarkably reduced radiative recombination probability and an increased charge migration efficiency, as demonstrated by the photoluminescence (PL) spectroscopy (Fig. S5b) and electrochemical impedance spectroscopy (EIS, Fig. S5c). These results indicate that the introduction of atomically dispersed Cu in TiO_2 not only provides the underlying active sites for photocatalytic CO_2 reduction reaction, but also broadens light response region and enhances the charge separation/transfer efficiencies.

3.2. Dioxygen-enhanced photocatalytic CO_2 reduction performance

The performance of Cu-SAs/ TiO_2 photocatalyst for CO_2 reduction is evaluated in a gas-solid heterogeneous photocatalytic system under the simulated sunlight from Xe lamp. Pure TiO_2 only produces CO with a very slow evolution rate of $2.68\text{ }\mu\text{mol}\cdot\text{g}_{\text{cat}}^{-1}\cdot\text{h}^{-1}$; while the optimal Cu-SAs/ TiO_2 photocatalyst affords the coproduction of CH_4 and CO, with significantly enhanced evolution rates of 23.11 and $13.71\text{ }\mu\text{mol}\cdot\text{g}_{\text{cat}}^{-1}\cdot\text{h}^{-1}$ (0–2 h), respectively (Fig. S6). H_2 is not produced in this photocatalytic system (Fig. S7). However, the long-term photocatalytic reaction (Fig. 2a) demonstrates that the activity of Cu-SAs/ TiO_2 catalyst declines observably with the prolonged illumination time, meaning that the photocatalyst is deactivated gradually during CO_2 photoreduction. The Cu-SAs/ TiO_2 photocatalyst also shows a color variation from light green to brown (Fig. S8a and S8b). The activity declination of Cu-SAs/ TiO_2 photocatalyst for CO_2 reduction should be caused by the transformation of $\text{Cu}^{\delta+}$ to metallic Cu⁰ under continuous light irradiation [18,23]. However, it is delightfully found that the Cu-SAs/ TiO_2 catalyst can perform stably in the long-time photocatalytic CO_2 reduction reaction after feeding a small amount of O_2 (117.6 ppm) into the reaction system (Fig. 2b), and the color of Cu-SAs/ TiO_2 remains almost unchanged after the photocatalytic reaction (Fig. S8c), indicating that the presence of molecular oxygen can stabilize the chemical state of $\text{Cu}^{\delta+}$ active sites. After the optimization of O_2 concentration in the reaction system, the Cu-SAs/ TiO_2 photocatalyst exhibits the best CO_2 reduction performance in the presence of 117.6 ppm O_2 (Fig. 2c and Fig. S9). In terms of the total CO_2 conversion to fuel (CH_4 and CO), the addition of 117.6 ppm O_2 increases the total yield of fuel up to nearly 1.5 folds, and the selectivity of CH_4 rises from 58.90% to 59.56%, compared with the case without O_2 . Notably, the production rates of CH_4 and CO at the initial stage of photocatalytic CO_2 reduction reaction (from 0 to 2 h, Fig. S10a) are promoted by introducing 117.6 ppm O_2 , and this superiority is particularly pronounced after a long-time photocatalytic reaction (from 9 to 10 h, Fig. S10b). These results indicate that the activity of Cu-SAs/ TiO_2 photocatalyst is not only maintained well but also further enhanced in the photocatalytic CO_2 reduction reaction with a small amount of O_2 , suggesting that the molecular O_2 has play a crucial role to accelerate CO_2 photoreduction. Even so, the average production rates are still lower at later reaction times than in the first 2 h reaction time (Fig. S10), probably because the replenishment of reactants fails to keep pace with their consumptions on photocatalyst. When the O_2 concentration is 2932.6 ppm, only CO is produced over Cu-SAs/ TiO_2 photocatalyst with a very slow rate of $4.56\text{ }\mu\text{mol}\cdot\text{g}_{\text{cat}}^{-1}\cdot\text{h}^{-1}$ (Fig. S9d). In the presence of excess O_2 , the Cu active sites are occupied by O_2 adsorption, which

greatly hinders the adsorption of CO_2 and results in a decreased CO_2 reduction performance.

In addition, the control experiments under different conditions (Figs. 2d and S11) verify that the detected products are indeed derived from the photocatalytic reaction between CO_2 and H_2O . The photocatalytic CO_2 reduction reaction is conducted under the same conditions (117.6 ppm O_2) with deionized water (DI water) to replace ethanol for preparing the catalyst film (Fig. S12), which confirms that the ethanol dispersion has no effect on the assessment of photocatalytic CO_2 reduction performance. Furthermore, the isotope labeling experiment (Figs. 2e and S13) is carried out by using $^{13}\text{CO}_2$ as the carbon source and keeping other conditions unchanged. The results confirm that the detected products are derived from the reduction of $^{13}\text{CO}_2$, excluding the possibility that the products are from the pollutants adsorbed on photocatalyst. The cycling test is also carried out on the Cu-SAs/ TiO_2 photocatalyst to further demonstrate its high stability under the conditions of photocatalytic CO_2 reduction reaction in the presence of 117.6 ppm O_2 . As shown in Fig. 2f, both activity and selectivity of the photocatalytic CO_2 reduction to CH_4 and CO are maintained very well after 5 cycles totaling 50 h light irradiation, confirming the favorable durability of the photocatalyst under the present reaction conditions. Therefore, the appropriate presence of O_2 can improves both activity and stability of the Cu-SAs/ TiO_2 photocatalyst in CO_2 reduction reaction.

3.3. Experimental investigations on the role of O_2 in promoting CO_2 photoreduction

In order to probe the variation in the chemical state of Cu sites during the photocatalytic reaction, low-temperature (77 K) electron paramagnetic resonance (EPR) spectra of Cu-SAs/ TiO_2 catalyst are measured before and after light irradiation (Fig. 3a). The Cu-SAs/ TiO_2 sample shows a characteristic EPR signal of Cu^{2+} ($g_{\parallel}=2.33$, $g_{\perp}=2.06$) [19,37]. After 10 min light irradiation, the signal intensity of Cu^{2+} decreases obviously, probably because some of Cu^{2+} sites are reduced into EPR-silent Cu^+ species. Furthermore, XPS measurements are performed on the Cu-SAs/ TiO_2 catalyst under different conditions (Figs. 3b and S14). In comparison, the 2p-orbital binding energies of Cu sites in Cu-SAs/ TiO_2 catalyst present a little negative shift after the photocatalytic CO_2 reduction reaction in the absence of O_2 , suggesting the partial reduction of $\text{Cu}^{\delta+}$ sites to low oxidation states during photocatalytic process. The binding energies of Ti 2p orbital shift positively by 0.2 eV after the photocatalytic reaction without O_2 (Fig. S14), indicating the electron transfer from TiO_2 to Cu. In contrast, both the binding energies of Cu 2p and Ti 2p in the Cu-SAs/ TiO_2 catalyst present a little positive shift after photocatalytic CO_2 reduction in the presence of O_2 . These results demonstrate that the photogenerated electrons are readily transferred from TiO_2 to $\text{Cu}^{\delta+}$ sites during photocatalytic process and the stored electrons in $\text{Cu}^{\delta+}$ sites migrate towards the chemisorbed O_2 molecules to maintain the chemical state of $\text{Cu}^{\delta+}$ on TiO_2 . Therefore, the Cu-SAs/ TiO_2 catalyst has an improved stability during photocatalytic CO_2 reduction reaction with a small amount of O_2 .

Since the infrared vibration frequency of chemisorbed CO molecules is very sensitive to the chemical environment of surface metal sites, the light-induced evolutions in Cu chemical states of Cu-SAs/ TiO_2 catalyst under different conditions (without or with O_2) are tracked by *in-situ* CO diffuse reflectance infrared Fourier transform spectroscopy (*in-situ* CO-DRIFTS). Fig. 3c shows the *in-situ* CO-DRIFTS of Cu-SAs/ TiO_2 sample measured in the absence of O_2 under Xe-lamp irradiation. The infrared signals appearing in the region of $2200\text{--}1800\text{ cm}^{-1}$ are assignable to the chemisorbed CO on Cu^{2+} or Cu^+ sites of Cu-SAs/ TiO_2 catalyst after Ar purging [38]. The broad band in the region of $2200\text{--}2150\text{ cm}^{-1}$ is ascribed to the vibration frequency of CO coordinated to Cu^{2+} sites [39, 40], which disappears rapidly under light irradiation. Meanwhile, the peaks (2100 cm^{-1} and 2050 cm^{-1}) related to the chemisorbed CO on Cu^+ sites are enhanced gradually. Moreover, the broad band in the

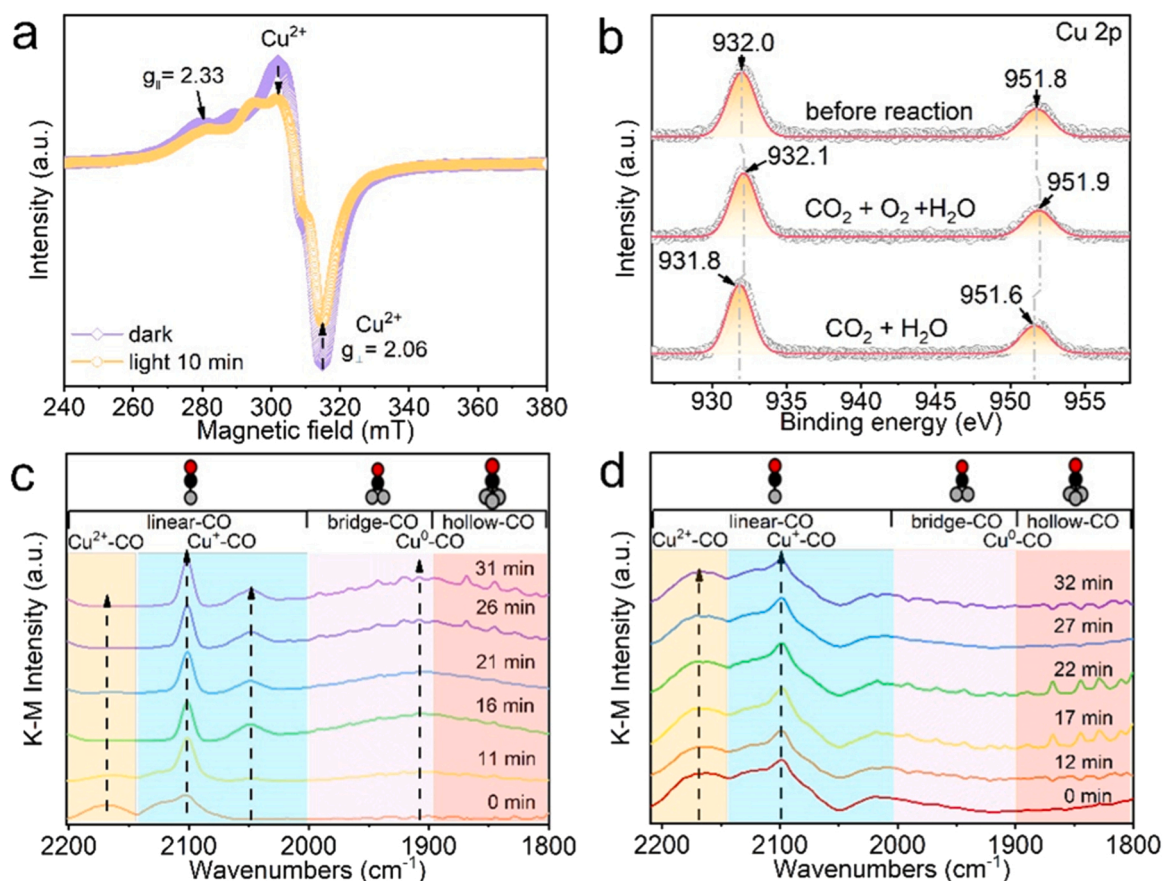


Fig. 3. (a) Low temperature (77 K) EPR spectra of Cu-SAs/TiO₂ before (violet line) and after (yellow line) light irradiation. (b) XPS spectra of Cu 2p before and after photocatalytic CO₂ reaction. *In-situ* CO-DRIFTS for probing the change of Cu chemical states (c) without O₂ and (d) with 117.6 ppm O₂.

region of 2000–1800 cm^{-1} assignable to the CO adsorbed on Cu^0 sites (bridge adsorption: 2000–1900 cm^{-1} , hollow adsorption: 1900–1800 cm^{-1}) appears and becomes more obvious with the prolonged irradiation time [41,42]. These results suggest that in the absence of O₂, the Cu^{2+} active sites on Cu-SAs/TiO₂ catalyst will be inevitably reduced to Cu^0 under a long-time light irradiation, which is responsible for the deactivation of Cu-SAs/TiO₂ photocatalyst in a long-term CO₂ reduction process. When a small amount of O₂ (117.6 ppm) is introduced into the chamber for *in-situ* CO-DRIFTS measurement, the infrared vibration frequencies of chemisorbed CO molecules on Cu-SAs/TiO₂ catalyst are almost unchanged during the light irradiation process, as shown in Fig. 3d, indicating that the chemical states of Cu^{2+} sites can be stabilized by adsorbing a proper amount of O₂. As a result, both *in situ* EPR and *in situ* CO-DRIFTS characterizations consistently prove the crucial role of O₂ in stabilizing Cu^{2+} sites on Cu-SAs/TiO₂ catalyst, which governs the activity and selectivity of the photocatalytic CO₂ reduction reaction.

To probe the evolution of O₂ during photocatalytic CO₂ reduction process, the reactive oxygen species (ROS) generated in the reaction systems under different atmospheres (pure CO₂, CO₂ + O₂, pure O₂) are identified by using 3,3',5,5'-tetramethylbenzidine (TMB) as a probe molecule. The experimental details are described in Supporting Information. The colorless TMB ($\lambda_{\text{max}} = 285 \text{ nm}$) can be converted into a blue charge-transfer complex with characteristic absorption peaks at 370 and 652 nm through the one-electron oxidation by active oxygen species ($\cdot\text{O}_2$, $\text{OH}\cdot$, H_2O_2 , etc.) [25], as shown in Fig. S15. Compared with the result in pure CO₂ atmosphere (Fig. 4a), the TMB oxidation rates in O₂ + CO₂ system and pure O₂ system are significantly accelerated (Figs. 4b and S16a), indicating that more ROSs are generated by Cu-SAs/TiO₂ photocatalyst in the presence of O₂ even though the O₂ concentration is

as low as 117.6 ppm (Fig. 4b). Furthermore, several typical scavengers like superoxide dismutase (SOD), mannitol and catalase are added in the reaction system to eliminate superoxide radical ($\cdot\text{O}_2$), hydroxyl radical ($\cdot\text{OH}$) and H_2O_2 [43], respectively. In pure CO₂ atmosphere (Fig. 4a), the addition of mannitol can totally suppress TMB oxidation, suggesting that $\cdot\text{OH}$ is a dominant ROS generated during the photocatalytic process under pure CO₂ atmosphere. Besides, the addition of catalase also leads to an obvious suppression in TMB oxidation, related to the formation of H_2O_2 in this photocatalytic system which is probably from the transformation of $\cdot\text{OH}$. The TMB oxidation is barely affected by the addition of SOD, meaning that $\cdot\text{O}_2$ is hardly generated in the photocatalytic reaction system without O₂. The corresponding results from O₂ + CO₂ or pure O₂ systems manifest the joint contribution of several different ROSs including $\cdot\text{O}_2$, $\cdot\text{OH}$ and H_2O_2 , where $\cdot\text{O}_2$ should be generated by the competitive electron transfer from Cu^{2+} sites to O₂ adsorbed on Cu-SAs/TiO₂ photocatalyst. The generation of H_2O_2 in the photocatalytic CO₂ reduction systems without and with O₂ have been detected by the iodimetry method (Fig. S16b–d), respectively, which affirm that the presence of O₂ accelerates the generation of H_2O_2 in photocatalytic CO₂ reduction reaction. It should be noted that the detected H_2O_2 amounts are far less than the theoretical yields because the decomposition of H_2O_2 is inevitable during the photocatalytic process. The competitive electron transfer from Cu^{2+} sites to O₂ on Cu-SAs/TiO₂ photocatalyst is beneficial to the dynamic stability of Cu^{2+} active sites in a long-term photocatalytic CO₂ reduction. Moreover, the generation of $\cdot\text{O}_2$ radical may facilitate H_2O dissociation and proton transfer, thus promoting the CO₂ reduction reaction [44,45].

The generation of $\cdot\text{OOH}$ intermediate on Cu-SAs/TiO₂ photocatalyst is evidenced by *in-situ* DRIFTS. The mixed gas of O₂ and H₂O are introduced into the vacuumed chamber containing Cu-SAs/TiO₂

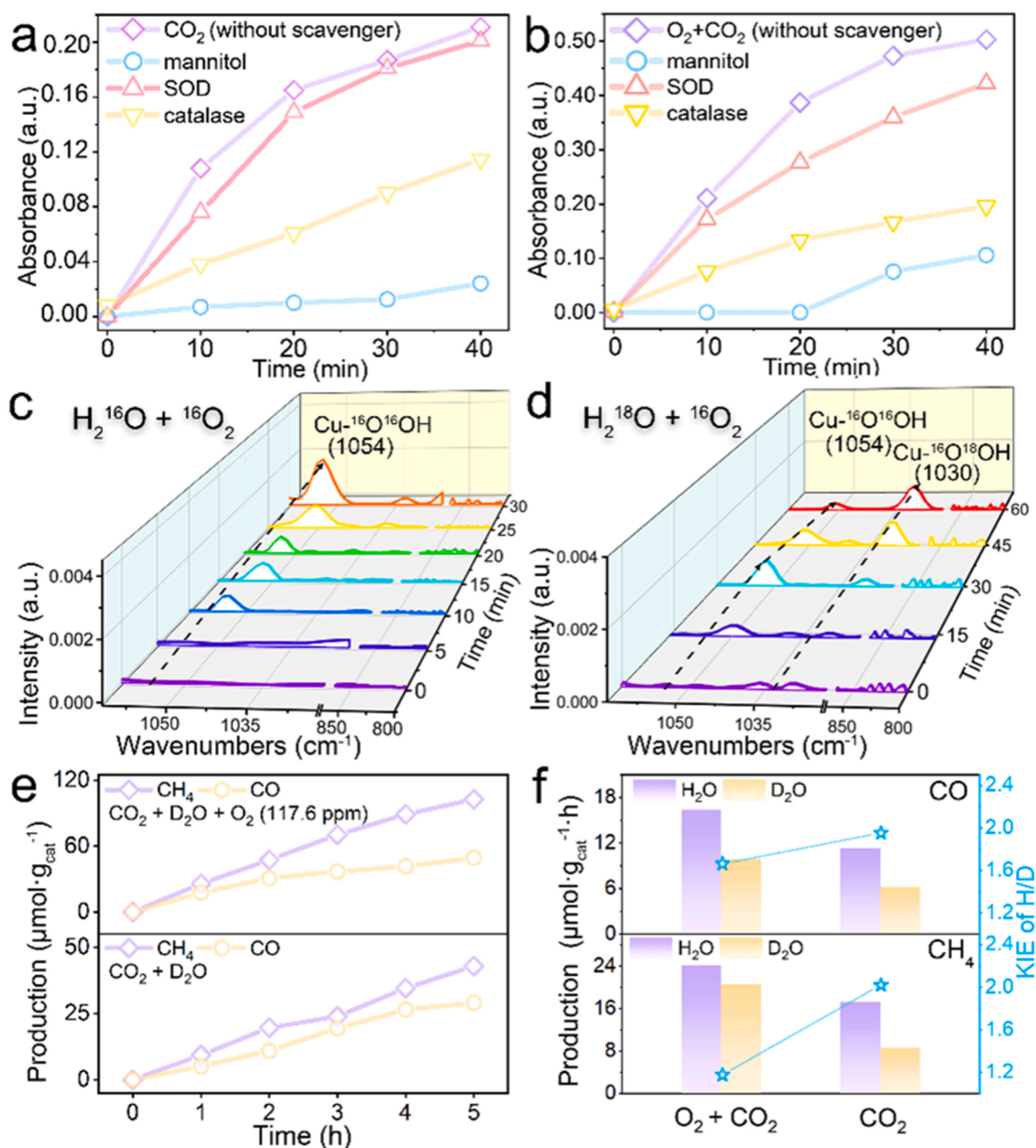


Fig. 4. UV-vis absorbance intensity for TMB oxidation vs. reaction time over Cu-SAs/TiO₂ photocatalyst under (a) pure CO₂ and (b) O₂(117.6 ppm) + CO₂ atmosphere with adding different scavengers. (c-d) *In situ* DRIFTS of Cu-SAs/TiO₂ photocatalyst in the presence of O₂ and H₂¹⁶O (H₂¹⁸O) under light irradiation. (e) Time-dependent product yields over Cu-SAs/TiO₂ photocatalyst for CO₂ + D₂O + O₂ (117.6 ppm) and CO₂ + D₂O reaction systems. (f) The KIE values of H/D and the production rates of CH₄ and CO over Cu-SAs/TiO₂ photocatalyst.

photocatalyst, and the background spectrum is collected after adsorption equilibrium. The time-dependent DRIFTS spectra are recorded under the irradiation of Xe lamp to track the evolution of surface-bound species. As shown in Fig. 4c, it is interestingly found that a prominent absorption band appears at 1054 cm⁻¹ for Cu-SAs/TiO₂ catalyst in the presence of O₂ and H₂O under light irradiation, suggesting the emergence of a key intermediate. According to previous reports [46,47], the gradually pronounced absorption band at ~1054 cm⁻¹ can be tentatively assigned to the surface superoxide *OOH intermediate. Considering that the characteristic infrared absorption band of Ti-OOH is located at ~837 cm⁻¹ [48,49], the band at 1054 cm⁻¹ should be related to the-OOH species bound on Cu sites. To confirm this hypothesis, the ¹⁸O isotope-labeled *in-situ* DRIFTS experiments are conducted for the Cu-SAs/TiO₂ photocatalyst by using H₂¹⁸O to replace H₂¹⁶O (Fig. 4d).

Previous study has demonstrated that the characteristic infrared absorption bands of partially labeled (¹⁶O-¹⁸O) and fully labeled (¹⁸O-¹⁸O) groups generally have a shift of 20–30 cm⁻¹ and 44–61 cm⁻¹ [46,50], respectively. Therefore, it is reasonable that the band at 1054 cm⁻¹ corresponds to the vibration frequency of -¹⁶O¹⁶OH and the band at 1030 cm⁻¹ is related to the vibration frequency of -¹⁶O¹⁸OH (Fig. 4d). In comparison, no infrared absorption band appears prominently in the absence of H₂O and O₂ for Cu-SAs/TiO₂ catalyst under the same light irradiation (Fig. S17), which consolidates the formation of-OOH intermediate from photocatalytic transformation of O₂ and H₂O on Cu-SAs/TiO₂ catalyst. These results indicate that the molecular oxygen adsorbed on Cu^{δ+} sites of Cu-SAs/TiO₂ photocatalyst would undergo a series of oxygen activation steps via-O₂ and-OOH intermediates. Specifically, the O₂ adsorbed on Cu sites of photocatalyst can acquire

photogenerated electrons accumulated in Cu sites to form $\cdot\text{O}_2^-$. The $\cdot\text{O}_2^-$ radical is liable to seizure a proton from H_2O [51] and develops into $\cdot\text{OOH}$ intermediate. This process is conducive to promoting water dissociation and supplying protons for CO_2 reduction. The influence of O_2 on water dissociation to deliver hydrogen for CO_2 reduction is studied by the kinetic isotope effect (KIE) of H/D in photocatalytic CO_2 reduction reaction with Cu-SAs/ TiO_2 catalyst (Fig. 4e-f). The KIE value can be used as an indicator of proton-transfer from water dissociation during CO_2 protonation process [52,53]. The KIE values of photocatalytic CO_2 reduction to CH_4 and CO are 2.02 and 1.95, respectively, indicating that water dissociation is largely restricted when D_2O is used as a proton source to replace H_2O . In the presence of 117.6 ppm O_2 , the KIE values sharply decrease to 1.17 and 1.66, meaning that the water dissociation almost ceases to affect the rate-determining step of photocatalytic CO_2 reduction. Therefore, the appropriate existence of O_2 can promote water dissociation and accelerate the rate-determining step of CO_2 protonation.

To track the intermediate evolutions of photocatalytic CO_2 reduction process in the presence of O_2 and further disclose the roles of O_2 in this process, *in-situ* DRIFTS experiments are conducted for the photocatalytic CO_2 reduction reaction over Cu-SAs/ TiO_2 catalyst with introducing different O_2 concentrations (Figs. 5a and S18). For the coexistence of CO_2 , H_2O and O_2 (117.6 ppm) over Cu-SAs/ TiO_2 catalyst, several infrared absorption bands appear and increase gradually under the continuous light irradiation, as shown in Fig. 5a. The accumulation of carbonate species on Cu-SAs/ TiO_2 catalyst before light irradiation (0 min) is evidenced by the emergence of infrared signals at 1400 cm^{-1} (monodentate carbonate, m-CO_3^{2-}) and 1537 cm^{-1} (bidentate carbonate, b-CO_3^{2-}) [54], which are derived from the preliminary interaction of the adsorbed CO_2 and H_2O on catalyst [54–56]. The absorption band at 1645 cm^{-1} appears and dominates gradually in the spectrum with the extension of illumination time, corresponding to the rapid generation of $\cdot\text{COOH}$ intermediate (“*” denotes the active sites of catalyst) [54]. Meanwhile, the infrared absorption in $2200\text{--}1800\text{ cm}^{-1}$ rises slowly, which is ascribable to the formation of $\cdot\text{CO}$ species bound on Cu sites, and the weak absorption band in $3000\text{--}2600\text{ cm}^{-1}$ is related to $\cdot\text{CHO}$ species [15,57]. Moreover, the band of the C–H vibration frequency of methyl at 1296 cm^{-1} appears for producing CH_4 under continuous illumination [58,59]. Compared with the O_2 -free and O_2 -excessive (2932.6 ppm) cases shown in Fig. S18, the photocatalytic CO_2 reduction system with 117.6 ppm O_2 shows the fastest generation rates of intermediate species, affirming the significant promoting effect of appropriate O_2 on photocatalytic CO_2 reduction reaction. This is also evidenced by the more prominent EPR signals (Fig. S19) of radical intermediates in the photocatalytic CO_2 reduction system with 117.6 ppm O_2 [23,60].

The all-around characterizations described above demonstrate that both stability and activity of Cu-SAs/ TiO_2 photocatalyst are significantly improved for photocatalytic CO_2 reduction by introducing a small amount of O_2 . The moderate adsorption of O_2 on photocatalyst surface can restrain the transformation of $\text{Cu}^{\delta+}$ active sites to inactive Cu^0 owing to the electron migration from Cu sites to chemisorbed O_2 , thus keeping the dynamic stability of $\text{Cu}^{\delta+}$ active sites in a long-term photocatalytic process. Furthermore, the generated $\cdot\text{O}_2^-$ radical can promote H_2O dissociation to form $\cdot\text{OOH}$ intermediate which accelerates the proton-coupled electron transfer process of CO_2 reduction, resulting in the enhanced yield rates of CH_4 and CO as well as a higher selectivity for CH_4 production.

3.4. Theoretical calculations on photocatalytic mechanism

Density functional theory (DFT) calculations are conducted to provide the theoretical evidence on the O_2 -enhanced performance of Cu-SAs/ TiO_2 catalyst in photocatalytic CO_2 reduction reaction. Based on the experimental characterizations, the surface structure of Cu single-atom anchored TiO_2 (101) (Cu-SA/ TiO_2) is constructed (Fig. S20),

where the monatomic Cu prefers to locate at five coordination position than the six-coordination position with the energy difference of $\Delta E = -0.39\text{ eV}$. Besides, oxygen vacancies are introduced on pure TiO_2 (101) surface and Cu-SA/ TiO_2 surface respectively, involving O_2 -vacancy and O_3 -vacancy. The calculation shows that Cu-SA/ TiO_2 ($E_{\text{O}_2\text{CV}} = 0.33\text{ eV}$ and $E_{\text{O}_3\text{CV}} = 2.06\text{ eV}$) is more likely to form oxygen vacancies than pure TiO_2 (101) surface ($E_{\text{O}_2\text{CV}} = 5.13\text{ eV}$ and $E_{\text{O}_3\text{CV}} = 5.45\text{ eV}$) (Figs. S21 and S22). It is easier to form two-coordination oxygen vacancies on the surface of Cu-SA/ TiO_2 , and therefore the Cu-SA/ TiO_2 surface with two-coordination oxygen vacancy is used as catalyst model to study the related photocatalytic mechanism.

Since photocatalytic CO_2 reduction generally follows the proton-coupled electron transfer (PCET) pathway [61,62], herein the reaction pathway is investigated based on PCET process. Firstly, the transfer of proton and electron from H_2O to the Cu-SA/ TiO_2 surface proceeds with an energy barrier of 0.31 eV (Fig. S23). Some of the critical challenges in specific to the CO_2 reduction reaction lie in the intrinsic stability of CO_2 molecule ($\Delta G = 394.39\text{ kJ mol}^{-1}$) and the high energy required to break the C–O bonds [63]. The one-electron photocatalytic CO_2 reduction to $\cdot\text{CO}_2$ has a high redox potential ($E^0 = -1.85\text{ V}$ vs. NHE under $\text{pH} = 7$), which is not achievable for most semiconductors [64]. The initial protonation steps for CO_2 to $\cdot\text{COOH}$ intermediate thermodynamically requires a reaction energy of 0.50 eV (Fig. 5b), and kinetically the activation energy is 0.53 eV for the formation of $\cdot\text{COOH}$ (Fig. 5c). The $\cdot\text{COOH}$ intermediate is prone to decompose into $\cdot\text{CO}$ and H_2O with an uphill barrier of 0.21 eV . Herein, the larger adsorption energy ($E_{\text{abs}} = -2.09\text{ eV}$, $d_{\text{C-Cu}} = 1.88\text{ \AA}$) stabilizes the adsorption configuration of $\cdot\text{COOH}$ and block the further hydrogenation on C site. The $\cdot\text{CO}$ tends to further hydrogenation to $\cdot\text{CHO}$ with a barrier of 1.17 eV rather than the desorption from Cu site ($E_{\text{abs}} = -1.66\text{ eV}$, $d_{\text{C-Cu}} = 1.908\text{ \AA}$). The $\cdot\text{CHO}$ is further hydrogenated with a barrier of 0.80 eV to form $\cdot\text{CHOH}$, which splits into $\cdot\text{CH}$ and H_2O with a tiny energetic penalty of 0.07 eV for C–O bond fracture ($E_a = 0.16\text{ eV}$). The successive hydrogenation of $\cdot\text{CH} \rightarrow \cdot\text{CH}_2 \rightarrow \cdot\text{CH}_3 \rightarrow \cdot\text{CH}_4$ occurs under the barriers of 1.06 eV , 0.32 eV and 0.79 eV respectively. The weak adsorption ($E_{\text{abs}} = 0.32\text{ eV}$, $\Delta G = 0.39\text{ eV}$) demonstrates that the CH_4 product can be easily desorbed from the catalyst. The formation of the C–H bond in $\cdot\text{CHO}$ with the highest barrier ($E_a = 1.17\text{ eV}$) is the rate-limiting step in the entire reaction from CO_2 to CH_4 . Although the reaction speed of CO hydrogenation to $\cdot\text{CHO}$ is faster than the CO desorption speed, a small amount of CO molecules will be generated inevitably. In addition, as shown in Fig. 5b, the formation of CH_4 ($\Delta G_{\text{max}} = 0.77\text{ eV}$) is more thermodynamically than the formation of CO ($\Delta G_{\text{max}} = 1.54\text{ eV}$). Thus, Cu-SA/ TiO_2 photocatalytic conversion of CO_2 to CH_4 has a higher selectivity than CO .

Subsequently, both the O_2 reduction and the CO_2 reduction in the presence of O_2 are calculated, respectively, to investigate the effect of O_2 on the photocatalytic CO_2 reduction reaction. As shown in Fig. S25, O_2 ($E_{\text{abs}} = -1.68\text{ eV}$) is more liable to be adsorbed on Cu-SA/ TiO_2 surface than CO_2 ($E_{\text{abs}} = -0.38\text{ eV}$). Via the Langmuir–Hinshelwood (LH) mechanism, the activated $\cdot\text{O}_2$ kinetically goes through an uphill process of 0.23 eV energy barrier to generate $\cdot\text{OOH}$, which can be further rapidly reduced to generate H_2O_2 (Fig. S26). In comparison, the co-adsorption of O_2 and CO_2 on Cu site shows the most negative adsorption energy ($E_{\text{abs}} = -1.81\text{ eV}$, Fig. S25), indicating that the presence of O_2 strengthens CO_2 adsorption. The adsorbed O_2 on Cu site attains the activation state ($d_{\text{O-O}} = 1.286\text{ \AA}$, Bader charge = $0.3437e$), while CO_2 appears to be not obviously activated ($d_{\text{C-O}} = 1.178\text{ \AA}$, $\angle\text{CO}_2 = 179.89^\circ$, Bader charge = $0.001e$). However, with the aid of $\cdot\text{OOH}$, CO_2 can be promoted to produce $\cdot\text{COOH}$ with the energy barrier of 0.25 eV (Fig. 5c), which is much lower than that of CO_2 reduction in the absence of O_2 ($E_a = 0.53\text{ eV}$). Meanwhile, O_2 adsorbed at the Cu site continues to be hydrogenated into $\cdot\text{OOH}$ ($E_a = 0.14\text{ eV}$), which is further reduced to H_2O_2 ($E_a = 0.01\text{ eV}$) and desorbed from the surface of catalyst. The formation of $\cdot\text{COOH}$ in photocatalytic CO_2 reduction reaction is usually considered as a crucial step, which is greatly promoted on Cu-SA/ TiO_2 surface in the presence of $\cdot\text{OOH}$. As a result, the reaction mechanism of

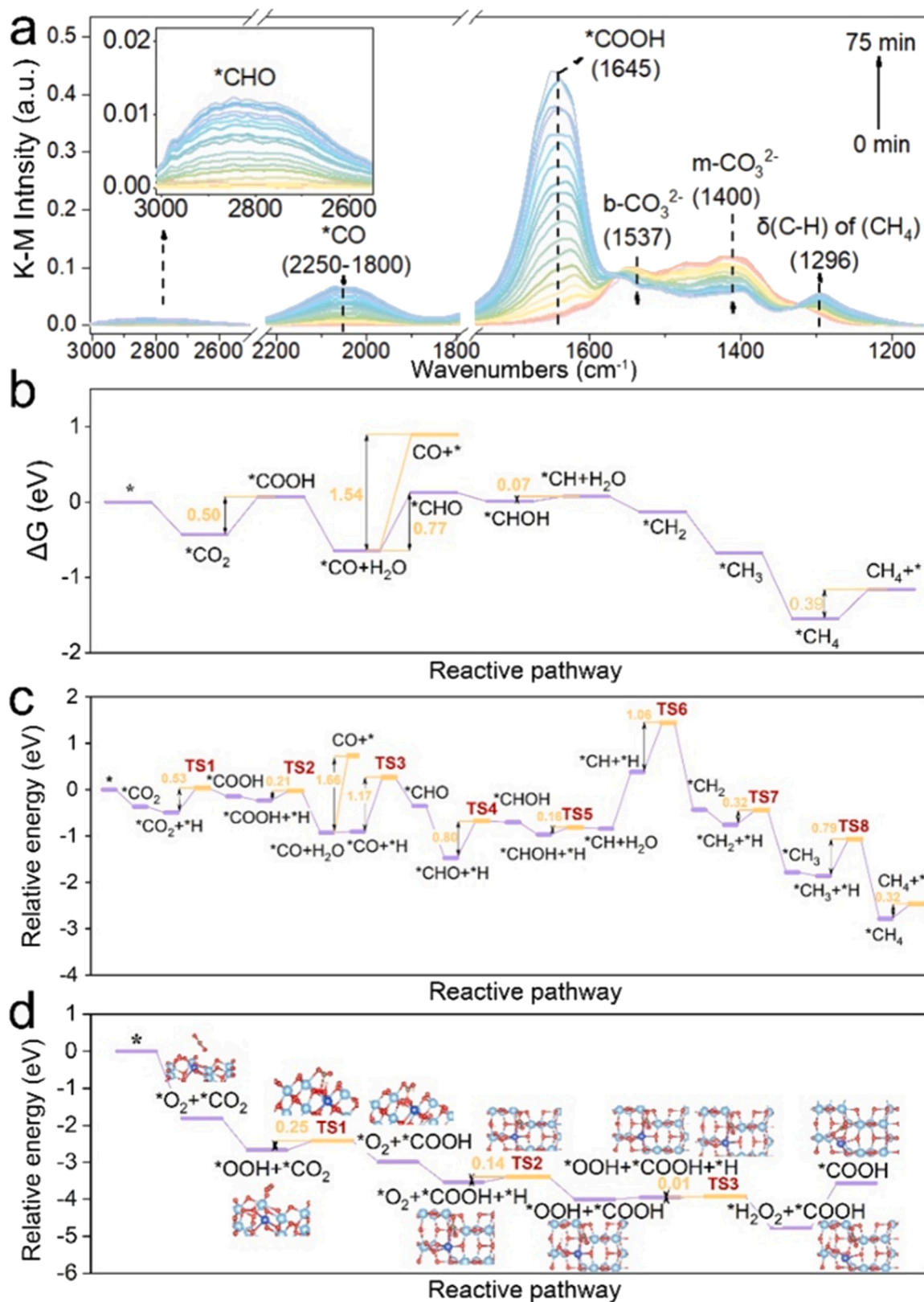


Fig. 5. (a) *In-situ* DRIFTS of photocatalytic CO_2 reduction in the presence of 117.6 ppm O_2 . (b) Gibbs free energies and (c) the kinetic energy barriers of photocatalytic CO_2 reduction on Cu-SA/ TiO_2 surface (the corresponding configurations are shown in Fig. S24), (d) the partial reaction path of photocatalytic CO_2 reduction in the presence of O_2 on Cu-SA/ TiO_2 surface.

photocatalytic CO₂ reduction on Cu-SAs/TiO₂ catalyst with a small amount of O₂ is illustrated in Fig. 6 and the possible reaction paths are shown in Fig. S27. Up the photoexcitation of Cu-SAs/TiO₂ catalyst, the O₂ adsorbed on Cu site acquires a photogenerated electron to generate $\cdot\text{O}_2^-$, and the $\cdot\text{O}_2^-$ radical seizes a proton from the adsorbed H₂O to form $\cdot\text{OOH}$ intermediate. Since the transformation of $\cdot\text{OOH}$ to H₂O₂ is feasible while the decomposition of H₂O₂ is inevitable, the adsorbed O₂ probably goes through a series of transformations like $\cdot\text{O}_2^- + \text{H}^+ \leftrightarrow \cdot\text{OOH} \leftrightarrow \text{H}_2\text{O}_2$ during the photocatalytic process. The easy shifts between $\cdot\text{O}_2^-$ and $\cdot\text{OOH}$ facilitate the proton transfer to the activated CO₂ and their derived intermediates on Cu sites, accelerating the proton-coupled electron transfer pathway of CO₂ reduction. Moreover, the appropriate adsorption of O₂ on Cu-SAs/TiO₂ catalyst surface can restrain the reduction of Cu^{δ+} active sites to inactive Cu⁰ owing to the electron migration from Cu to chemisorbed O₂, thus keeping the dynamic stability of Cu^{δ+} active sites in a long-term photocatalytic process.

4. Conclusions

In summary, this study demonstrated a facile fabrication of porous TiO₂ supported Cu SAs catalyst and the O₂-enhanced photocatalytic performance in CO₂ reduction. Both activity and stability of Cu-SAs/TiO₂ catalyst were greatly improved in photocatalytic CO₂ reduction reaction by introducing a small amount of O₂ (117.6 ppm), enabling the solar fuel production to increase from 23.41 to 34.64 μmol·g⁻¹·h⁻¹. XPS, *in situ* EPR and CO-DRIFTS measurements showed that the presence of O₂ could stabilize Cu^{δ+} sites on Cu-SAs/TiO₂ catalyst. A series of experimental identifications indicated that $\cdot\text{O}_2^-$ was generated by the competitive electron transfer from Cu^{δ+} sites to O₂ on Cu-SAs/TiO₂ photocatalyst, and $\cdot\text{O}_2^-$ was subsequently converted to $\cdot\text{OOH}$ intermediate. The competitive electron transfer could maintain the dynamic stability of Cu^{δ+} active sites in a long-term photocatalytic process. Moreover, the generation of $\cdot\text{O}_2^-$ and $\cdot\text{OOH}$ species facilitated H₂O dissociation to afford sufficient protons for CO₂ reduction, which was evidenced by the kinetic isotope effect. Using DFT calculations, we assessed the reaction energies of O₂ reduction on Cu-SA/TiO₂ surface as well as the reaction energies of the key steps for the generation and transformation of the $\cdot\text{COOH}$ intermediate in the absence/presence of O₂. The calculation results showed that the molecular O₂ was preferentially activated into $\cdot\text{OOH}$ in the co-existence of O₂ and CO₂ on Cu-SA/TiO₂ surface, and the presence of $\cdot\text{OOH}$ could promote the transformation of CO₂ to $\cdot\text{COOH}$ with an energy barrier of 0.25 eV which is much lower than the corresponding energy barrier in the absence of O₂ ($E_a = 0.53$ eV). Therefore, the appropriate presence of O₂ could stabilize the favorable chemical state of Cu^{δ+} active sites as well as accelerate the proton-coupled electron transfer process of CO₂ reduction, resulting in the high yield rates of solar fuel, together with the greatly enhanced durability of photocatalyst. This work provides a strategy to convert the CO₂ feedstock mixed with a small amount of O₂ to carbon-neutral fuel with high conversion rate. The previous studies on CO₂ reduction reaction generally use pure CO₂ or CO₂-N₂ mixture as the reactant gas. However, CO₂ feedstock mixed with a small amount of O₂ can be obtained at a lower cost in industrial processes. The CO₂ purification process can be simplified when the CO₂ stream mixed with a small amount of O₂ is used as reactant directly for solar fuel with high conversion rate.

CRediT authorship contribution statement

Ting Wang: Investigation, Methodology, Data curation, Software, Writing – original draft. **Fuli Sun:** Methodology, Data curation, Software, Validation, Writing – original draft. **Shoujie Liu:** Methodology, Software, Validation. **Guilin Zhuang:** Methodology, Software, Writing – review & editing. **Benxia Li:** Supervision, Conceptualization, Writing – review & editing, Funding acquisition.

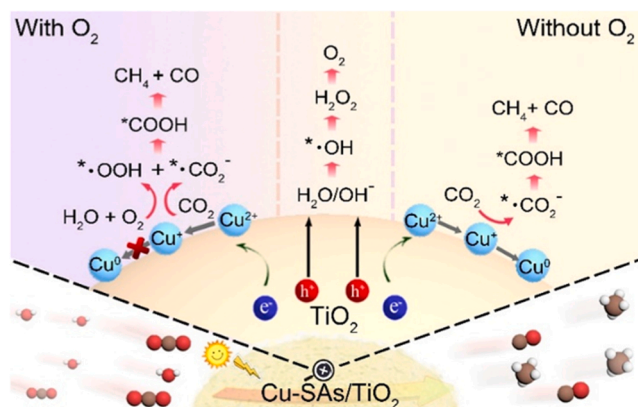


Fig. 6. The diagram of possible reaction mechanism for photocatalytic CO₂ reduction over Cu-SAs/TiO₂ catalyst with and without O₂, respectively.

Declaration of Competing Interest

The authors declare that they have no known competing financial interests or personal relationships that could have appeared to influence the work reported in this paper.

Data availability

Data will be made available on request.

Acknowledgments

This work was supported by the National Natural Science Foundation of China (21471004, 22022108), the Fundamental Research Funds of Zhejiang Sci-Tech University (2020Y003) and the Science Foundation of Zhejiang Sci-Tech University (17062002-Y).

Appendix A. Supporting information

Supplementary data associated with this article can be found in the online version at doi:10.1016/j.apcatb.2022.122339.

References

- [1] R. Schäppi, D. Rutz, F. Dähler, A. Muroyama, P. Haueter, J. Lilliestam, A. Patt, P. Furler, A. Steinfeld, Drop-in fuels from sunlight and air, *Nature* 601 (2021) 63–68.
- [2] H. Lin, S. Luo, H. Zhang, J. Ye, Toward solar-driven carbon recycling, *Joule* 6 (2022) 294–314.
- [3] H. Rao, L.C.S. Chmidt, J. Bonin, M. Robert, Visible-light-driven methane formation from CO₂ with a molecular iron catalyst, *Nature* 548 (2017) 74–77.
- [4] B.H. Lee, E. Gong, M. Kim, S. Park, H.R. Kim, J. Lee, E. Jung, C.W. Lee, J. Bok, Y. Jung, Y.S. Kim, K.S. Lee, S.P. Cho, J.W. Jung, C.H. Cho, S. Lebegue, K.T. Nam, H. Kim, S.I. In, T. Hyeon, Electronic interaction between transition metal single-atoms and anatase TiO₂ boosts CO₂ photoreduction with H₂O, *Energy Environ. Sci.* 15 (2022) 601–609.
- [5] C. Gao, Y.J. Xiong, Solar-driven artificial carbon cycle, *Chin. J. Chem.* 40 (2022) 153–159.
- [6] Y. Zhang, E. Chen, J. Tang, Insight on reaction pathways of photocatalytic CO₂ conversion, *ACS Catal.* 12 (2022) 7300–7316.
- [7] R.F. Tang, X.A. Dong, J.P. Sheng, S.B. Xi, L.L. Zhang, F. Dong, Single-metal catalytic sites via high-throughput mechanochemistry enable selective and efficient CO₂ photoreduction, *Appl. Catal. B-Environ.* 316 (2022), 121661.
- [8] S.J. Xie, Y.F. Li, B. Sheng, W.Y. Zhang, W. Wang, C.C. Chen, J.K. Li, H. Sheng, J. C. Zhao, Self-reconstruction of paddle-wheel copper-node to facilitate the photocatalytic CO₂ reduction to ethane, *Appl. Catal. B-Environ.* 310 (2022), 121320.
- [9] Y. Zhang, B. Xia, J. Ran, K. Davey, S.Z. Qiao, Atomic-level reactive sites for semiconductor-based photocatalytic CO₂ reduction, *Adv. Energy Mater.* 10 (2020), 1903879.
- [10] Q. Li, Y.X. Gao, M. Zhang, H. Gao, J. Chen, H.P. Jia, Efficient infrared-light-driven photothermal CO₂ reduction over MOF-derived defective Ni/TiO₂, *Appl. Catal. B-Environ.* 303 (2022), 120905.
- [11] Z.Q. Wang, J.C. Zhu, X.L. Zu, Y. Wu, S. Shang, P.Q. Ling, P.Z. Qiao, C.Y. Liu, J. Hu, Y. Pan, J.F. Zhu, Y.F. Sun, Y. Xie, Selective CO₂ photoreduction to CH₄ via Pd^{δ+}-

- assisted hydrodeoxygenation over CeO₂ nanosheets, *Angew. Chem. Int. Ed.* 61 (2022), e202203249.
- [12] Y.B. Feng, C. Wang, P.X. Cui, C. Li, B. Zhang, L.Y. Gan, S.B. Zhang, X.X. Zhang, X. Y. Zhou, Z.M. Sun, K.W. Wang, Y.Y. Duan, H. Li, K. Zhou, H.W. Huang, A. Li, C. Q. Zhuang, L.H. Wang, Z. Zhang, X.D. Han, Ultrahigh photocatalytic CO₂ reduction efficiency and selectivity manipulation by single-tungsten-atom oxide at the atomic step of TiO₂, *Adv. Mater.* 34 (2022), 2109074.
- [13] X.L. Jin, Y.X. Xu, X. Zhou, C.D. Lv, Q.Z. Huang, G. Chen, H.Q. Xie, T. Ge, J. Cao, J. Q. Zhan, L.Q. Ye, Single-atom Fe triggers superb CO₂ photoreduction on a bismuth-rich catalyst, *ACS Mater. Lett.* 3 (2021) 364–371.
- [14] S.F. Ji, Y. Qu, T. Wang, Y.J. Chen, G.F. Wang, X. Li, J.C. Dong, Q.Y. Chen, W. Y. Zhang, Z.D. Zhang, S.Y. Liang, R. Yu, Y. Wang, D.S. Wang, Y.D. Li, Rare-earth single erbium atoms for enhanced photocatalytic CO₂ reduction, *Angew. Chem. Int. Ed.* 59 (2020) 10651–10657.
- [15] Y.Y. Yu, X.A. Dong, P. Chen, Q. Geng, H. Wang, J.Y. Li, Y. Zhou, F. Dong, Synergistic effect of Cu single atoms and Au-Cu alloy nanoparticles on TiO₂ for efficient CO₂ photoreduction, *ACS Nano* 15 (2021) 14453–14464.
- [16] Y. Zhou, Y. Yao, R. Zhao, X. Wang, Z. Fu, D. Wang, H. Wang, L. Zhao, W. Ni, Z. Yang, Y.-M. Yan, Stabilization of Cu⁺ via strong electronic interaction for selective and stable CO₂ electroreduction, *Angew. Chem. Int. Ed.* 61 (2022), e202205832.
- [17] Y.A. Wu, I. McNulty, C. Liu, K.C. Lau, Q. Liu, A.P. Paulikas, C.J. Sun, Z.H. Cai, J. R. Guest, Y. Ren, V. Stamenkovic, L.A. Curtiss, Y.Z. Liu, T. Rajh, Facet-dependent active sites of a single Cu₂O particle photocatalyst for CO₂ reduction to methanol, *Nat. Energy* 4 (2019) 957–968.
- [18] L. Yuan, S.F. Hung, Z.R. Tang, H.M. Chen, Y.J. Xiong, Y.J. Xu, Dynamic evolution of atomically dispersed Cu species for CO₂ photoreduction to solar fuels, *ACS Catal.* 9 (2019) 4824–4833.
- [19] B.H. Lee, S. Park, M. Kim, A.K. Sinha, S.C. Lee, E. Jung, W.J. Chang, K.S. Lee, J. H. Kim, S.P. Cho, H. Kim, K.T. Nam, T. Hyeon, Reversible and cooperative photoactivation of single-atom Cu/TiO₂ photocatalysts, *Nat. Mater.* 18 (2019) 620–626.
- [20] T. Wang, L. Chen, C. Chen, M. Huang, Y. Huang, S. Liu, B. Li, Engineering catalytic interfaces in Cu^{+/0}/CeO₂-TiO₂ photocatalysts for synergistically boosting CO₂ reduction to ethylene, *ACS Nano* 16 (2022) 2306–2318.
- [21] J.F. Zhang, Y. Wang, Z.Y. Li, S. Xia, R. Cai, L. Ma, T.Y. Zhang, O. Ackley, S.Z. Yang, Y.C. Wu, J.J. Wu, Grain boundary-derived Cu^{+/0} interfaces in CuO nanosheets for low overpotential carbon dioxide electroreduction to ethylene, *Adv. Sci.* (2022), 2200454.
- [22] X.Z. Su, Z.L. Jiang, J. Zhou, H.J. Liu, D.N. Zhou, H.S. Shang, X.M. Ni, Z. Peng, F. Yang, W.X. Chen, Z.M. Qi, D.S. Wang, Y. Wang, Complementary operando spectroscopy identification of in-situ generated metastable charge-asymmetry Cu₂-Cu₃ clusters for CO₂ reduction to ethanol, *Nat. Commun.* 13 (2022) 1322.
- [23] S. Kreft, R. Schoch, J. Schneidewind, J. Rabeah, E.V. Kondratenko, V. A. Kondratenko, H. Junge, M. Bauer, S. Wohlrab, M. Beller, Improving selectivity and activity of CO₂ reduction photocatalysts with oxygen, *Chem* 5 (2019) 1818–1833.
- [24] T. Wang, X. Tao, Y. Xiao, G. Qiu, Y. Yang, B. Li, Charge separation and molecule activation promoted by Pd/MIL-125-NH₂ hybrid structures for selective oxidation reactions, *Catal. Sci. Technol.* 10 (2020) 138–146.
- [25] X. Sun, X. Luo, X.D. Zhang, J.F. Xie, S. Jin, H. Wang, X.S. Zheng, X.J. Wu, Y. Xie, Enhanced superoxide generation on defective surfaces for selective photooxidation, *J. Am. Chem. Soc.* 141 (2019) 3797–3801.
- [26] O. Tomita, T. Otsubo, M. Higashi, B. Ohtani, R. Abe, Partial oxidation of alcohols on visible-light-responsive WO₃ photocatalysts loaded with palladium oxide cocatalyst, *ACS Catal.* 6 (2016) 1134–1144.
- [27] X. Tao, R. Long, D. Wu, Y. Hu, G. Qiu, Z. Qi, B. Li, R. Jiang, Y. Xiong, Anchoring positively charged Pd single atoms in ordered porous ceria to boost catalytic activity and stability in suzuki coupling reactions, *Small* 16 (2020), 2001782.
- [28] Y.J. Chen, S.F. Ji, W.M. Sun, Y.P. Lei, Q.C. Wang, A. Li, W.X. Chen, G. Zhou, Z. D. Zhang, Y. Wang, L.R. Zheng, Q.H. Zhang, L. Gu, X.D. Han, D.S. Wang, Y.D. Li, Engineering the atomic interface with single platinum atoms for enhanced photocatalytic hydrogen production, *Angew. Chem. Int. Ed.* 59 (2020) 1295–1301.
- [29] A.A. Liu, L.C. Liu, Y. Cao, J.M. Wang, R. Si, F. Gao, L. Dong, Controlling dynamic structural transformation of atomically dispersed CuO_x species and influence on their catalytic performances, *ACS Catal.* 9 (2019) 9840–9851.
- [30] L. Liu, A. Corma, Identification of the active sites in supported subnanometric metal catalysts, *Nat. Catal.* 4 (2021) 453–456.
- [31] X. Deng, R. Li, S.K. Wu, L. Wang, J.H. Hu, J. Ma, W.B. Jiang, N. Zhang, X.S. Zheng, C. Gao, L.J. Wang, Q. Zhang, J.F. Zhu, Y.J. Xiong, Metal-organic framework coating enhances the performance of Cu₂O in photoelectrochemical CO₂ reduction, *J. Am. Chem. Soc.* 141 (2019) 10924–10929.
- [32] M. Xiao, L. Zhang, B. Luo, M.Q. Lyu, Z.L. Wang, H.M. Huang, S.C. Wang, A.J. Du, L. Z. Wang, Molten-salt-mediated synthesis of an atomic nickel co-catalyst on TiO₂ for improved photocatalytic H₂ evolution, *Angew. Chem. Int. Ed.* 59 (2020) 7230–7234.
- [33] F. Tian, Y. Zhang, J. Zhang, C. Pan, Raman spectroscopy: A new approach to measure the percentage of anatase TiO₂ exposed (001) facets, *J. Phys. Chem. C* 116 (2012) 7515–7519.
- [34] Y.X. Zhao, Y.F. Zhao, R. Shi, B. Wang, G.I.N. Waterhouse, L.Z. Wu, C.H. Tung, T. R. Zhang, Tuning oxygen vacancies in ultrathin TiO₂ nanosheets to boost photocatalytic nitrogen fixation up to 700 nm, *Adv. Mater.* 31 (2019), e1806482.
- [35] G.H. Yin, X.Y. Huang, T.Y. Chen, W. Zhao, Q.Y. Bi, J. Xu, Y.F. Han, F.Q. Huang, Hydrogenated blue titania for efficient solar to chemical conversions: Preparation, characterization, and reaction mechanism of CO₂ reduction, *ACS Catal.* 8 (2018) 1009–1017.
- [36] Z. Wang, D. Brouri, S. Casale, L. Delannoy, C. Louis, Exploration of the preparation of Cu/TiO₂ catalysts by deposition-precipitation with urea for selective hydrogenation of unsaturated hydrocarbons, *J. Catal.* 340 (2016) 95–106.
- [37] Y.M. Zhang, J.H. Zhao, H. Wang, B. Xiao, W. Zhang, X.B. Zhao, T.P. Lv, M. Thangamuthu, J. Zhang, Y. Guo, J.N. Ma, L.N. Lin, J.W. Tang, R. Huang, Q. J. Liu, Single-atom Cu anchored catalysts for photocatalytic renewable H₂ production with a quantum efficiency of 56%, *Nat. Commun.* 13 (2022) 58.
- [38] T. Yang, X.N. Mao, Y. Zhang, X.P. Wu, L. Wang, M.Y. Chu, C.W. Pao, S.Z. Yang, Y. Xu, X.Q. Huang, Coordination tailoring of Cu single sites on C₃N₄ realizes selective CO₂ hydrogenation at low temperature, *Nat. Commun.* 12 (2021) 6022.
- [39] W. Wang, C.Y. Deng, S.J. Xie, Y.F. Li, W.Y. Zhang, H. Sheng, C.C. Chen, J.C. Zhao, Photocatalytic C-C coupling from carbon dioxide reduction on copper oxide with mixed-valence copper(I)/copper(II), *J. Am. Chem. Soc.* 143 (2021) 2984–2993.
- [40] C.M. Gunathunge, J.Y. Li, X. Li, J.L.J. Hong, M.M. Waeglele, Revealing the predominant surface facets of rough Cu electrodes under electrochemical conditions, *ACS Catal.* 10 (2020) 6908–6923.
- [41] Z.X. Tao, A.J. Pearce, J.M. Mayer, H.L. Wang, Bridge sites of Au surfaces are active for electrocatalytic CO₂ reduction, *J. Am. Chem. Soc.* 144 (2022) 8641–8648.
- [42] Z. Tan, M. Haneda, H. Kitagawa, B. Huang, Slow synthesis methodology-directed immiscible octahedral Pd₁Rh_{1-x} dual-atom-site catalysts for superior three-way catalytic activities over Rh, *Angew. Chem. Int. Ed.* 61 (2022), e202202588.
- [43] H. Wang, D.Y. Yong, S.C. Chen, S.L. Jiang, X.D. Zhang, W. Shao, Q. Zhang, W. S. Yan, B.C. Pan, Y. Xie, Oxygen-vacancy-mediated exciton dissociation in BiOBr for boosting charge-carrier-involved molecular oxygen activation, *J. Am. Chem. Soc.* 140 (2018) 1760–1766.
- [44] M. He, C.S. Li, H.C. Zhang, X.X. Chang, J.G.G. Chen, W.A. Goddard, M.J. Cheng, B. J. Xu, Q. Lu, Oxygen induced promotion of electrochemical reduction of CO₂ via co-electrolysis, *Nat. Commun.* 11 (2020) 3844.
- [45] T.M. Tran-Thuy, C.C. Chen, S.D. Lin, Spectroscopic studies of how moisture enhances CO oxidation over Au/BN at ambient temperature, *ACS Catal.* 7 (2017) 4304–4312.
- [46] W.R. Cheng, X. Zhao, H. Su, F.M. Tang, W. Che, H. Zhang, Q.H. Liu, Lattice-strained metal-organic-framework arrays for bifunctional oxygen electrocatalysis, *Nat. Energy* 4 (2019) 115–122.
- [47] H. Su, W.L. Zhou, W. Zhou, Y.L. Li, L.R. Zheng, H. Zhang, M.H. Liu, X.X. Zhang, X. Sun, Y.Z. Xu, F.C. Hu, J. Zhang, T.D. Hu, Q.H. Liu, S.Q. Wei, In-situ spectroscopic observation of dynamic-coupling oxygen on atomically dispersed iridium electrocatalyst for acidic water oxidation, *Nat. Commun.* 12 (2021) 6118.
- [48] N. Sivasankar, W.W. Weare, H. Frei, Direct observation of a hydroperoxide surface intermediate upon visible light-driven water oxidation at an Ir oxide nanocluster catalyst by rapid-scan FT-IR spectroscopy, *J. Am. Chem. Soc.* 133 (2011) 12976–12979.
- [49] R. Nakamura, A. Imanishi, K. Murakoshi, Y. Nakato, In situ FTIR studies of primary intermediates of photocatalytic reactions on nanocrystalline TiO₂ films in contact with aqueous solutions, *J. Am. Chem. Soc.* 125 (2003) 7443–7450.
- [50] E. McCandlish, A.R. Miskztal, M. Nappa, A.Q. Sprenger, J.S. Valentine, J.D. Stong, T.G. Spiro, Reactions of superoxide with iron porphyrins in aprotic solvents. A high spin ferric porphyrin peroxo complex, *J. Am. Chem. Soc.* 102 (1980) 4268–4271.
- [51] J.C. Liu, Y. Tang, C.R. Chang, Y.G. Wang, J. Li, Mechanistic insights into propene epoxidation with O₂-H₂O mixture on Au₇/α-Al₂O₃: A hydroperoxyl pathway from ab initio molecular dynamics simulations, *ACS Catal.* 6 (2016) 2525–2535.
- [52] J.C. Zhu, W.W. Shao, X.D. Li, X.C. Jiao, J.F. Zhu, Y.F. Sun, Y. Xie, Asymmetric triple-atom sites confined in ternary oxide enabling selective CO₂ photothermal reduction to acetate, *J. Am. Chem. Soc.* 143 (2021) 18233–18241.
- [53] P.G. Liu, Z.X. Huang, X.P. Gao, X. Hong, J.F. Zhu, G.M. Wang, Y.E. Wu, J. Zeng, X. S. Zheng, Synergy between palladium single atoms and nanoparticles via hydrogen spillover for enhancing CO₂ photoreduction to CH₄, *Adv. Mater.* 34 (2022), 2200057.
- [54] J.P. Sheng, Y. He, J.Y. Li, C.W. Yuan, H.W. Huang, S.Y. Wang, Y.J. Sun, Z.M. Wang, F. Dong, Identification of halogen-associated active sites on bismuth-based perovskite quantum dots for efficient and selective CO₂-to-CO photoreduction, *ACS Nano* 14 (2020) 13103–13114.
- [55] K. Wang, R.M. Jiang, T. Peng, X. Chen, W.X. Dai, X.Z. Fu, Modeling the effect of Cu doped TiO₂ with carbon dots on CO₂ methanation by H₂O in a photo-thermal system, *Appl. Catal. B-Environ.* 256 (2019), 117780.
- [56] X.H. Lin, S.B. Wang, W.G. Tu, Z.B. Hu, Z.X. Ding, Y.D. Hou, R. Xu, W.X. Dai, MOF-derived hierarchical hollow spheres composed of carbon-confined Ni nanoparticles for efficient CO₂ methanation, *Catal. Sci. Technol.* 9 (2019) 731–738.
- [57] W.C. Ma, S.J. Xie, T.T. Liu, Q.Y. Fan, J.Y. Ye, F.F. Sun, Z. Jiang, Q.H. Zhang, J. Cheng, Y. Wang, Electrocatalytic reduction of CO₂ to ethylene and ethanol through hydrogen-assisted C-C coupling over fluorine-modified copper, *Nat. Catal.* 3 (2020) 478–487.
- [58] Y.L. He, F.C. Guo, K.R. Yang, J.A. Heinlein, S.M. Bamente, J.J. Fee, S. Hu, S.L. Suib, G.L. Haller, V.S. Batista, L.D. Pfefferle, In situ identification of reaction intermediates and mechanistic understandings of methane oxidation over hematite: A combined experimental and theoretical study, *J. Am. Chem. Soc.* 142 (2020) 17119–17130.
- [59] W. Zhang, C. Fu, J. Low, D. Duan, J. Ma, W. Jiang, Y. Chen, H. Liu, Z. Qi, R. Long, Y. Yao, X. Li, H. Zhang, Z. Liu, J. Yang, Z. Zou, Y. Xiong, High-performance photocatalytic nonoxidative conversion of methane to ethane and hydrogen by heteroatoms-engineered TiO₂, *Nat. Commun.* 13 (2022) 2806.
- [60] L. Fan, X. Bai, C. Xia, X. Zhang, X. Zhao, Y. Xia, Z.-Y. Wu, Y. Lu, Y. Liu, H. Wang, CO₂/carbonate-mediated electrochemical water oxidation to hydrogen peroxide, *Nat. Commun.* 13 (2022) 2668.

- [61] T.T. Kong, Y.W. Jiang, Y.J. Xiong, Photocatalytic CO₂ conversion: What can we learn from conventional CO_x hydrogenation? *Chem. Soc. Rev.* 49 (2020) 6579–6591.
- [62] S.Z. Xu, E.A. Carter, Theoretical insights into heterogeneous (photo) electrochemical CO₂ reduction, *Chem. Rev.* 119 (2019) 6631–6669.
- [63] X. Li, J.G. Yu, M. Jaroniec, X.B. Chen, Cocatalysts for selective photoreduction of CO₂ into solar fuels, *Chem. Rev.* 119 (2019) 3962–4179.
- [64] S.F. Ng, J.J. Foo, W.J. Ong, Solar-powered chemistry: Engineering low-dimensional carbon nitride-based nanostructures for selective CO₂ conversion to C₁-C₂ products, *InfoMat* 4 (2022), e12279.